Three-Dimensional Structure of the Corona During WHPI Campaign Rotations CR-2219 and CR-2223

D. G. Lloveras[1] [ORCID], **A. M. Vásquez[1,2], F. A. Nuevo[1,3], R. A. Frazin[4], W. Manchester IV[4], N. Sachdeva[4], B. Van der Holst[4], P. Lamy[5], and H. Gilardy[5]**

[1]Instituto de Astronomía y Física del Espacio, CONICET-UBA, Ciudad de Buenos Aires, Argentina, [2]Universidad Nacional de Tres de Febrero, Buenos Aires, Argentina, [3]Universidad de Buenos Aires, Ciclo Básico Común, Ciudad de Buenos Aires, Argentina, [4]Department of Climate and Space Sciences and Engineering, University of Michigan, Ann Arbor, MI, USA, [5]Laboratoire Atmosphéres, Milieux et Observations Spatiales, CNRS & UVSQ, Guyancourt, France

Abstract Differential emission measure tomography (DEMT) and white light (WL) tomography were applied to study the three-dimensional (3D) structure of the global solar corona for two Whole Heliosphere and Planetary Interactions campaign periods, Carrington rotations 2219 and 2223. With DEMT, Solar Dynamics Observatory/Atmospheric Imaging Assembly images were used to reconstruct the 3D coronal electron density and temperature in the range of heliocentric distance 1.02–1.25 $R_\odot$. With WL tomography, Solar and Heliospheric Observatory/Large Angle and Spectrometric COronagraph-C2 images were used to reconstruct the 3D electron density in the range of heliocentric distance 2.5–6.0 $R_\odot$. The two periods were also simulated with the 3D-magneto-hydrodynamic Alfvén Wave Solar Model (AWSoM), and its results compared in detail with the reconstructions. The DEMT analysis reveals a 20% less dense and 20% hotter corona than for rotations corresponding to the solar cycle 23/24 deep minimum. The electron density and temperature of the AWSoM model agree with DEMT results within 10% and 20%, respectively, while its electron density overestimates results of WL tomography up to 75%. The slow (fast) component of the terminal wind speed of the model is found to be associated with field lines characterized by larger (smaller) values of the tomographic density and temperature at the coronal base. DEMT reconstructions reveal the coronal plasma to be ubiquitously characterized by temperature variability of up to ≈45% over spatial scales of order ∼10^4 km. Taking into account this level of fine-structure by global models may be consequential for their predictions on wave propagation in the corona.

1. Introduction

The Whole Heliosphere and Planetary Interactions (WHPI) initiative, is an internationally coordinated observation and modeling effort focused on characterizing the three-dimensional (3D) heliosphere and the Sun-planetary relationship during the solar cycle (SC) 24/25 minimum epoch. The minimum of activity is of special interest because it allows the study and analysis of the solar corona in its simplest state. This global effort is preceded by the Whole Heliosphere Interval (WHI, Bisi et al., 2011) and the Whole Sun Month (WSM, Galvin & Kohl, 1999) campaigns, focused on studying the 2008 and the 1996 minima, respectively.

Towards the WHPI objectives, solar rotational tomography (SRT) is a valuable observational technique, able to provide a quantitative empirical description of the 3D distribution of fundamental plasma parameters of the solar corona at a global scale. The technique was originally developed by Altschuler and Perry (1972) to reconstruct the 3D distribution of the coronal electron density from white light (WL) coronagraph images. Later on, the differential emission measure tomography (DEMT) technique (Frazin et al., 2009) was developed, which applied to extreme ultraviolet (EUV) images allows reconstruction of the 3D distribution of both the electron density and temperature of the solar corona (Vásquez et al., 2009).

In this work, both WL-SRT and DEMT were used to study two specific WHPI campaign targets, the 2019 total solar eclipse Carrington rotation (CR)-2219 (2019, 29 June through 26 July), and the Parker Solar Probe and STEREO-A closest approach CR-2223 (2019, 16 October through 12 November). Both rotations provide snapshots of the evolving coronal structure as the solar activity approached its SC 24/25 minimum in December 2019. A modern implementation of SRT (Frazin & Janzen, 2002) was applied to WL polarization brightness (*pB*) images provided by the Solar and Heliospheric Observatory (SoHO) Large Angle and Spectrometric COronagraph (LASCO) C2 instrument, to obtain 3D reconstructions of the electron density of the corona in the

heliocentric height range 2.5–6.0 $R_\odot$. Also, DEMT was applied to EUV images provided by the Solar Dynamics Observatory (SDO) Atmospheric Imaging Assembly (AIA) instrument, to obtain 3D reconstructions of the electron density and temperature of the corona in the heliocentric height range 1.02–1.25 $R_\odot$.

In order to realistically and self-consistently model the solar corona and the solar wind, a common approach for global 3D magneto-hydrodynamic (MHD) models is to include an additional source term in the momentum equations, such as Alfvén waves as an empirical Wentzel-Kramers-Brillouin term (Ofman, 2010). An example of this general type of models is the Alfvén Wave Solar atmosphere Model (AWSoM), which is used in this work to model the solar corona. This global wave driven solar model considers the effect of dissipation of turbulence due to interaction between counter-propagating Alfvén waves (Van Doorsselaere et al., 2020). AWSoM is a self consistent 3D physics-based MHD model extending from the transition region to the upper corona and to 1 AU (Sokolov et al., 2013; van der Holst et al., 2010, 2014). The model is subject to continuous validation with observations as it is updated and improved. Sachdeva et al. (2019) compared the results of the model during a minimum of activity with DEMT and WL-SRT in a global fashion. The model has also been recently validated with DEMT reconstructions in different magnetic structures by Lloveras et al. (2020). More recently Sachdeva et al. (2021) conducted a validation study during solar maximum activity. In this work, the two selected WHPI rotations were simulated with steady-state AWSoM runs, whose results were compared with the tomographic reconstructions.

The previous WSM and WHI campaigns have been the subject of DEMT studies complemented with potential field source surface models of the global coronal magnetic field (Lloveras et al., 2017; Vásquez et al., 2011). In this work, the DEMT and WL-SRT results for the WHPI campaigns were traced along the magnetic field lines of the AWSoM model simulations, allowing to analyze the tomographic results in different magnetic structures, as well as to validate the model in different coronal regions and ranges of heliocentric height. Lamy et al. (2019) carried out a validation study of two 3D-MHD coronal models in a forward fashion, quantitatively comparing *pB* images from various coronagraphs against synthetic images calculated from the 3D electron density of the models. In this work, a similar quantitative validation of the AWSoM model was carried out by quantitatively comparing actual EUV and *pB* images with synthetic images computed from the 3D electron density and temperature of the model. The relationship between the terminal solar wind speed of the AWSoM model and the DEMT reconstructed electron density and temperature at the coronal base was also investigated.

In Section 2 the relevant aspects of the tomographic techniques and the AWSoM model are summarized. Section 3 shows, in 3D detail, the results of the tomographic reconstructions and the model, and their comparison. Section 4 summarizes and discusses the main conclusions of this analysis.

2. Methodology

2.1. WL-SRT and DEMT

Both WL-SRT and DEMT make use of time series of images of the solar corona (in wavelengths for which the corona is optically thin) taken from different view angles, as provided by solar rotation and the telescope's orbital motion. The time series is taken over a period of ≈1/2 synodic rotation to observe the full corona. In the case of the SoHO/LASCO-C2 and SDO/AIA instruments here used, both in nearly circular orbits of radius ≈1 a.u., this period is ≈14 days. The time series of data allows to pose a linear inversion problem to determine the 3D spatial distribution of specific parameters of the solar corona. The reconstruction is done over the range of heights covered by the telescope's field-of-view (FoV) where there is adequate signal strength.

The SRT technique applied in this work, for both WL-SRT and DEMT, assumes a static coronal structure. As a result, tomographic reconstructions are affected by dynamics-induced artifacts known as "zero density artifacts" (Frazin et al., 2009; Frazin & Janzen, 2002). ZDAs are non-reconstructed regions in the corona, and affect a relatively small coronal volume in solar minimum conditions such as in the WHPI rotations studied in this work. Mitigation of dynamics-induced artifacts in 3D tomography has been explored by Butala et al. (2010) using Kalman-filtering methods (Kalman, 1960). More recently Vibert et al. (2016) also investigated the use of spatio-temporal regularization of the solution. These methods have both been experimented in the case of WL tomography. Exploration of the benefits of their application to EUV tomography (used by DEMT) will be the focus of future efforts.

The coronal volume to be reconstructed is discretized on a spherical grid of N cells, whose size is set in relation to the resolution and FoV of the images and the cadence of the time series. The intensity values of each pixel of every image in the time series are arranged as a very large column vector of M intensity measurements. Each of those intensity values is the result of a line-of-sight (LOS) integral of an unknown coronal quantity times a known weighting factor which depends on the geometry of the observation and the emission mechanism. Specifically, in the case of WL-SRT the unknown is the coronal electron density, and in the case of EUV-SRT it is the coronal band's emissivity. Upon discretization, the LOS integral is transformed into a sum, and the column data vector of M intensities is equaled to a very large $M \times N$ projection matrix (containing only known terms depending on the observational geometry) multiplied by a column vector whose N elements are the unknown values of the coronal parameter to be found in each cell of the computational grid. The non-squared sparse projection matrix is non-invertible. The inversion is then posed as a multi-dimensional optimization problem with N unknowns, where the objective function is essentially the squared norm of the difference between the synthetic and actual data. Upon solving the optimization problem, the 3D distribution of the electron density or the EUV band emissivity is found in the case of WL-SRT and EUV-SRT, respectively.

In DEMT, the 3D EUV emissivity found in each of the telescope's bands is further used to solve for a local differential emission measure (DEM) problem. The local DEM, dubbed LDEM, describes the temperature distribution of the local plasma in each cell of the tomographic grid. The LDEM of each voxel is modeled as a Gaussian function $\text{LDEM}(T) = G(T; [T_0, \sigma_T, a])$, where T_0 is the centroid, σ_T its standard deviation, and a its amplitude. The parameters of the LDEM in each voxel are found by minimizing the discrepancy between the three tomographic values of the EUV band emissivity and the synthetic values computed from the LDEM (Vásquez et al., 2010). Once the LDEM is determined in a given voxel, its mean-squared electron density N_e^2, mean electron temperature T_e, and temperature spread W_T, are found by computing its zeroth through second moments,

$$N_e^2 = \int \text{LDEM}(T) \, dT, \tag{1}$$

$$T_e = \frac{1}{N_e^2} \int \text{LDEM}(T) \, T \, dT, \tag{2}$$

$$W_T^2 = \frac{1}{N_e^2} \int \text{LDEM}(T) \, (T - T_e)^2 \, dT. \tag{3}$$

In the expressions above, the integrals over temperature are carried out over the joint temperature sensitivity range [0.5, 3.0] MK of the three bands of AIA used in this work. DEMT studies systematically reveal that the coronal plasma is ubiquitously characterized by a significant temperature spread W_T within the volume of each voxel of characteristic linear size $\sim 10^4$ km (as detailed below).

For more details on SRT the reader is referred to Frazin and Janzen (2002), Vibert et al. (2016), and references therein. For further discussion on the DEMT technique and the LDEM, the reader is referred to Frazin et al. (2009); Vásquez et al. (2010); Nuevo et al. (2015). We detail next the specific setup used for SRT and DEMT in the tomographic reconstructions carried out in this work.

In the case of WL-SRT based on LASCO-C2 data, or C2-SRT hereafter, the tomographic problem is solved for the electron density of the corona. The 512^2 pixels LASCO-C2 images have a radial FoV of 2.5–6.0 $R_\odot$, so that the linear pixel size is $d \approx 0.02 \, R_\odot$. The size of the tomographic grid cell is set to $\Delta r = 0.1 \, R_\odot$ in the radial direction and $\Delta\theta = \Delta\phi = 3°$ in both the latitudinal (θ) and longitudinal (ϕ) directions. The average radial cell is located at a height $\langle r \rangle = 4.25 \, R_\odot$, and its angular linear size is then $\langle \Delta l \rangle = \langle r \rangle \times \Delta\theta \approx 0.2 \, R_\odot$. Taking into account the linear pixel size, the average cell in the plane-of-the-sky is then threaded by $\Delta r \times \langle \Delta l \rangle / d^2 \approx 50$ LOSs. Every LOS is numerically treated individually, and then a 16-fold binning is applied, so that the average cell is threaded by three 16-binned LOSs. As for cadence, for these grid a maximum of four images per day is possible, as the apparent rotation of the Sun is about the angular span of four angular cell sizes. In the case of LASCO-C2 we currently use one image per day, which is the available data. In experiments of C2-SRT carried out with different cadences, one image per day has been found to be optimal, as a larger cadence may introduce too many unreconstructed cells (ZDAs) due to coronal dynamics, so that 14 images have been used for each of the two rotations here studied. The $pB-$ images used in this work were obtained from the LASCO-C2 Legacy

Archive (http://idoc-lasco-c2-archive.ias.u-psud.fr), which provides images with the best-to-date calibration of the instrument (Lamy et al., 2020).

In the case of DEMT, EUV-SRT is applied to the 171, 193 and 211 Å bands of the AIA telescope (see Lloveras et al., 2020, for details), and the tomographic problem is solved for the each band emissivity of the corona. The 4096^2 pixels AIA images are first binned down to 1024^2 pixels, and have a radial FoV of 1.0–1.3 $R_\odot$, so that the linear pixel size is $d \approx 0.0025\ R_\odot$. The size of the tomographic grid cell is set to $\Delta r = 0.01\ R_\odot$ in the radial direction and $\Delta\theta = \Delta\phi = 2°$ in both the latitudinal (θ) and longitudinal (ϕ) directions. The average radial cell is located at a height $\langle r \rangle = 1.15\ R_\odot$, and its angular linear size is then $\langle \Delta l \rangle \approx 0.04\ R_\odot$. Taking into account the linear pixel size, the average cell in the plane-of-the-sky is then threaded by $\approx$64 LOSs. Every LOS is numerically treated individually, and then a 16-fold binning is applied, so that the average cell is threaded by four 16-binned LOSs. In the case of EUV-SRT a standard cadence of four images per day is used, so that 55 images have been used for each of the two rotations here studied. The AIA images used in this work were prepared using the up-to-date processing and calibration tools provided through the SolarSoftware package.

2.2. The AWSoM Model

AWSoM is a self-consistent 3D MHD model of the solar corona and inner heliosphere that addresses the heating of the solar corona by including low-frequency Alfvén wave turbulence, with proton temperature anisotropy, heat conduction, and radiative cooling to describe the solar wind. The extended MHD equations, which form the basis of the AWSoM model are described in detail inSokolov et al. (2013) and van der Holst et al. (2014), and validation results from an updated model can be found in Sachdeva et al. (2019) and Sachdeva et al. (2021). The MHD equations within AWSoM are solved using the Block-Adaptive-Tree-Solarwind-Roe-Upwind-Scheme (BATS-R-US, Powell et al., 1999). To simulate the Sun-Earth system, AWSoM comprises both the solar corona and the inner heliosphere components of the Space Weather Modeling Framework described in Tóth et al. (2012).

AWSoM is driven by the synoptic or synchronic maps derived from the observed photospheric magnetic, which are used to specify the radial magnetic field at the inner boundary of the model. Within the model, a Potential Field Source Surface Model (PFSSM) is used to extrapolate the 3D magnetic field from the observed photospheric field. The PFSSM may be specified using spherical harmonics or by numerical solution for the potential field. All three components of the magnetic field specify the initial conditions. The radial component specifies the boundary condition and is fixed according to the PFSSM solution while the longitudinal and latitudinal components of the magnetic field adjust freely according to the inner dynamics. The Alfvén wave energy density at the inner boundary is modeled with its Poynting flux scaling with the magnetic field. In the corona, the model considers wave reflection due to variation of the Alfvén speed along the propagation direction. Wave energy is specified propagating away from the boundary, while wave energy that impacts the boundary is absorbed. Finally, density and temperature are specified to be uniform.

These boundary conditions present limitations to accuracy of the model in two significant ways. Any synoptic map suffers from poor visibility at the solar poles. To compensate for this limitation, we use the synoptic magnetograms provided by application of the Air Force Data Assimilation Photospheric Flux Transport (ADAPT, Arge et al., 2013) model to synoptic maps of the Global Oscillation Network Group. These ADAPT-GONG maps provide a physics-based description of the unobserved polar magnetic fields by incorporating supergranulation, meridional circulation, and differential rotation. Like any solar coronal model, uncertainties in the observational data used to drive the model may propagate into the solution space as well. Limitations associated with the observations of photospheric magnetic field therefore may affect the AWSoM masodel output. The ADAPT model produces an ensemble of magnetic field maps that include uncertainty related to different model parameters. The ensemble modeling of the solar wind solutions can provide a set of solutions that can be compared to observations to find the best solution (see Sachdeva et al., 2019).

The proportionality constant between the Poynting flux of the outward propagating wave and the local magnetic field at the inner boundary is a free parameter of the model. During periods of increased magnetic activity, to reduce the excess energy deposited in the corona this factor is reduced as compared to its value of $10^6\ \mathrm{W\ m^{-2}\ T^{-1}}$ during solar minimum (Sachdeva et al., 2021). The Alfvén wave correlation length and the stochastic heating amplitude and exponent can also be adjusted to match the observations. For computational purposes, AWSoM makes use of an extended transition region, so that coronal conditions are achieved at heliocentric distance

$r \approx 1.05$ R$_\odot$. At the inner boundary, the initial electron and proton temperatures (both parallel and perpendicular) are set to 50,000 K. The proton number density is overestimated and set to 5×10^{18} m^{-3} for the model to be able to replenish the plasma that depletes due to chromospheric evaporation. This leads to an extending transition region as the AWSoM solution relaxes to equilibrium conditions slightly above the inner boundary.

Relevant to the analysis of this work is the model's 3D distribution of the electron density and temperature, the magnetic field, and the radial component of the solar wind velocity. A limitation of the density specification described above is that comparisons against tomographic reconstructions are possible only above $r = 1.05$ R$_\odot$. In its continuous development, the AWSoM model is the subject of validation efforts with observations both in the low corona and the heliosphere. In particular, WL-SRT and DEMT have both been used as part of validation studies (Jin et al., 2012; Lloveras et al., 2017, 2020; Oran et al., 2015; Sachdeva et al., 2019, 2021). The present study constitutes a new contribution in this series of works.

2.3. Results Along Magnetic Field Lines

Once the products of tomographic reconstructions (either C2-SRT or DEMT) are found, and the AWSoM model run has been calculated, the former are traced along the field lines of the latter, in order to characterize the global thermodynamic state of the solar corona in distinct magnetic structures. The method, previously applied by (Lloveras et al., 2020), is summarized next.

First, the geometry of sample field lines of the model is determined by numerical integration both inward and outward from starting points set at several heliocentric distances uniformly covering the range 1.02–1.25 R$_\odot$ in case of DEMT, and the range 2.5–6.0 R$_\odot$ in the case of C2-SRT. At each height one starting point is set every 2° in both latitude and longitude. This distribution of starting points allows to set magnetic field lines that sample the whole volume of the corona in the tomographic computational sphere.

Each traced magnetic field lines is classified as open or closed according to their full geometry. Closed magnetic field line were separated in two segments that extend from the coronal base up to the apex. For each traced open field line and for each segment of the closed field lines, simple functional fits are applied in order to characterize the traced tomographic results in a simple way.

In the case of DEMT, following the previous analysis by Lloveras et al. (2020), a hydrostatic isotermic fit is applied to the electron density as a function of height, and a linear fit is applied to the electron temperature as a function of height, which work well at the height range covered by the DEMT grid ($r \leq 1.25$ R$_\odot$). Specifically, the fits are described by the equations,

$$N_e^{(DEMT)}(r) = N_0 \exp\left[- (h/\lambda_N) \, / \, (r/R_\odot) \right], \tag{4}$$

$$T_e^{(DEMT)}(r) = T_0 + a\,h. \tag{5}$$

where in Equation 4, $h \equiv r - 1$ R$_\odot$ is the coronal height measured from the photosphere, λ_N [R$_\odot$] is the density scale height, and N_0 [cm^{-3}] is the electron density of the fit at $h = 0$. In Equation (5), the slope a [MK/R$_\odot$] is the radial temperature gradient, and T_0 [MK] is the electron temperature of the fit at $h = 0$.

In the case of C2-SRT, the radial FoV covered by the instrument (2.5–6.0 R$_\odot$) makes the hydrostatic regime less adequate to fit the electron density as a function of height. Previous works analyzing the large-scale coronal structure (Cairns et al., 2009; Guhathakurta et al., 1996; Harding et al., 2019; Kohl et al., 1998; Lobzin et al., 2008; Morgan, 2019; Sittler & Guhathakurta, 1999; Thernisien & Howard, 2006; Wang et al., 2017) use a combination of two or more power-law (PL) terms $\propto r^{-p}$, with different exponent values p to describe the observed trends of $N_e(r)$ over a wide range of heights r. In some cases a term r^{-2} is included to describe mass conservation of a constant speed radial outflow at very large values of r, while terms with larger exponents describe the observed trends over smaller values of r. In this work, an optimal goodness-of-fit to the observed $N_e(r)$ over the C2 FoV was found by using a single PL,

$$N_e^{(C2-SRT)}(r) = N_0\,(r/2.5\,\mathrm{R}_\odot)^{-p}, \tag{6}$$

where N_0 [cm^{-3}] is the electron density of the fit at $r = 2.5$ R$_\odot$ (the lowest height of the LASCO-C2 radial FoV), and p is the exponent. The characteristic scale height $\langle \lambda_N \rangle$ [R$_\odot$], height-averaged over the radial FoV, is a

Table 1
Classification of Traced Magnetic Field Lines According to Their Geometry (Open/Closed), Size (Small/Large, Upon Apex Being Within/Outside the Range of Heights of DEMT), Their Gradient of Temperature With Height (Up/Down, See Text), and the Footpoint Latitude θ_0

Type name	Open/Closed	Size	Up/Down	Footpoint latitude
0	Closed	Small	Down	$|\theta_0| < 50°$
I	Closed	Small	Up	$|\theta_0| < 50°$
II	Closed	Large	Up	$|\theta_0| > 40°$
III	Open	Large	Up	$|\theta_0| > 60°$

physically meaningful quantity that can then be calculated in a straightforward fashion as a function of the PL exponent,

$$\langle \lambda_N \rangle \equiv \left\langle \left| \frac{1}{N_e(r)} \frac{dN_e}{dr}(r) \right|^{-1} \right\rangle = \frac{\langle r \rangle}{p} = \frac{4.25\,R_\odot}{p}. \tag{7}$$

Once the fits have been applied for each traced field line, the statistical analysis of the results is carried out on the set of field lines that match the following criteria:

1. The field line must go through at least five tomographic grid cells with reconstructed data, and there must be at least one data point in each third of the range of heights spanned by the line. This requirement is set to ensure a reasonably spread sample of heights along the line.
2. The confidence level of the fit to the electron density, as well as to the electron temperature in the case of DEMT, must be larger than 90%.
3. In the case of DEMT, the correlation between temperature and heliocentric height must meet $|\rho(T, r)| > 0.5$, to ensure a linear fit is reasonable.

Based on their geometry an thermodynamical properties, the selected magnetic field lines are then classified in four different types, as indicated below. In the case of DEMT, closed loops are first classified as "small" or "large" depending on their apex being below or above the maximum height of the DEMT grid (1.25 $R_\odot$), respectively. Also in the case of DEMT, field lines (both closed and open) are further classified as "up" or "down" upon their fit to $T_e(r)$ increasing or decreasing with heliocentric height r, respectively. As shown in Section 3.1 below, the magnetically open/closed boundary of the AWSoM model for the simulated rotations is located always around latitude $\approx 60°$. Taking this into consideration, in order to separate different coronal structures based on their field line geometry and their thermodynamics, and similarly to the analysis by Lloveras et al. (2020), field lines are classified in the four types indicated in Table 1.

Section 3 shows in detail the statistical results of DEMT, C2-SRT, and AWSoM for the four classes of field lines here defined.

3. Results

3.1. DEMT Reconstructions and the AWSoM Model

For CRs 2219 and 2223, Figure 1 shows latitude-longitude maps of the electron density N_e and temperature T_e of both the DEMT analysis and the AWSoM model. Maps are shown at a sample heliocentric height $r = 1.105\,R_\odot$, in the middle of the range of heights covered by the DEMT computational grid. In the DEMT reconstructions, the larger density and temperature values that characterize the lower latitudes ($|\theta| \lesssim 60°$) correspond to the equatorial streamer belt, and the lower density and temperature at larger latitudes correspond to the coronal holes (CHs).

For both rotations, there is an overall good consistency between the AWSoM and DEMT maps, both in terms of shape and size of the streamer belt and the CHs, as well as in the characteristic values and their dynamic range. In the northern hemisphere, the location and shape of the open/closed (O/C) boundary of the AWSoM model closely matches the transition of the DEMT N_e from larger values in the streamer belt (red/yellow colors) to smaller CHs values (green/blue colors). The characteristic ratio of electron density between the streamer and the CHs is ≈ 2. Also across the O/C boundary, the DEMT temperature transitions from larger values within the streamer ($T_e \gtrsim 1.3$ MK) to lower values in the CHs ($T_e \lesssim 1.1$ MK). The characteristic values of both electron density and temperature, detailed in Figures 6 and 7 below, are consistent with those found in DEMT analysis or rotations selected from the previous two solar minima (Lloveras et al., 2017, 2020). In the southern hemisphere, also for both rotations, the agreement between DEMT results and the AWSoM model is similarly good in the range of Carrington longitudes $\approx 200–360°$, but is less satisfactory in the range of Carrington longitudes $\approx 0–200°$.

The value of the mean electron density N_e and temperature T_e in each voxel are found from the LDEM by means of Equations 1 and 2 which, as shown in Figure 1, result in different characteristic values in the streamer and CH regions. It is interesting to examine the typical LDEM temperature spread W_T in both regions as well, as
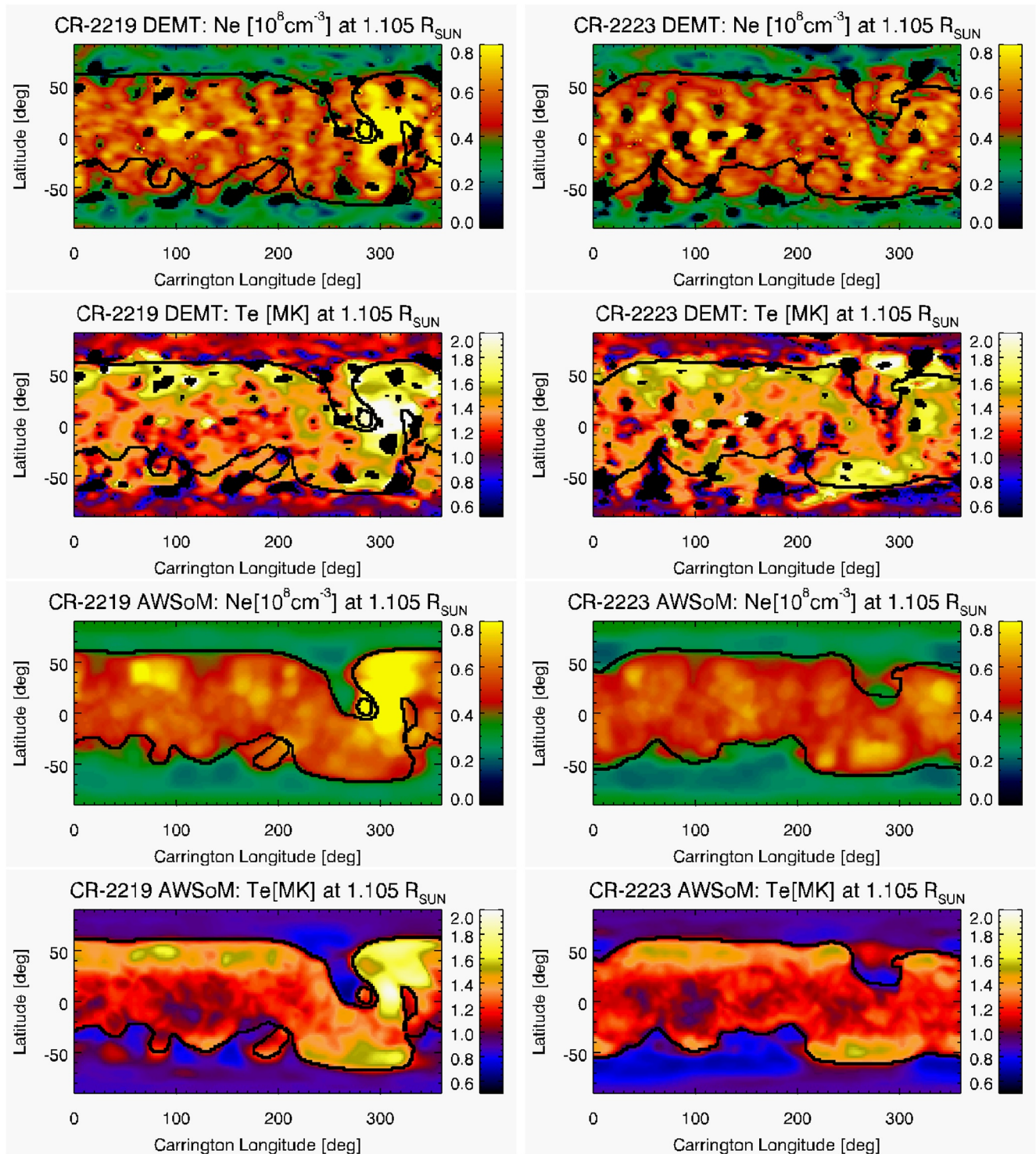
Figure 1. Latitude-longitude maps of electron density N_e and temperature T_e for CR-2219 (left panels) and CR-2223 (right panels) at heliocentric height 1.105 $R_\odot$ from differential emission measure tomography (DEMT) (top two panels) and from the Alfvén Wave Solar atmosphere Model (AWSoM) model (bottom two panels). Black pixels on DEMT maps correspond to non-reconstructed regions. In all maps, the thick-black curves indicate the boundaries between magnetically open and closed regions, based on the AWSoM model.
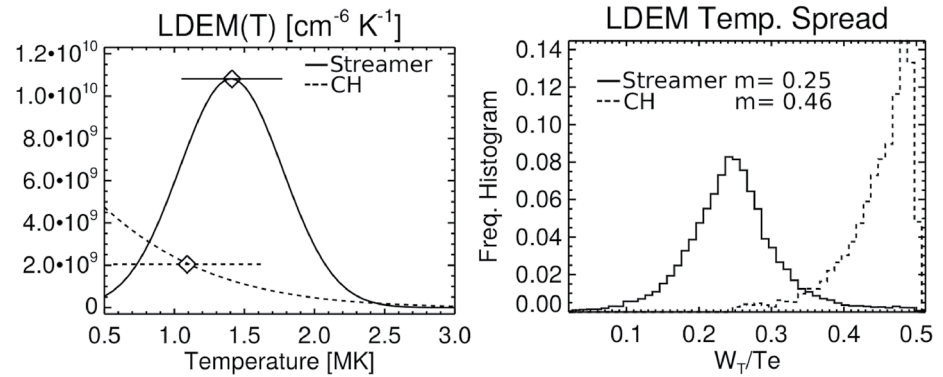
Figure 2. Left panel: characteristic example of LDEM in a tomographic cell corresponding to the streamer (solid line-style) and the CHs (dashed line-style). Over-plotted diamonds highlight the LDEM values at their respective mean electron temperature T_e, while the horizontal lines indicate the temperature spread $T_e \pm W_T$ of each LDEM. Right panel: statistical distribution of the relative temperature spread is W_T/T_e for all the tomographic voxels in both the streamer (solid line-style) and the CHs (dashed line-style).

determined from Equation 3. The left panel of Figure 2 shows a typical example of LDEM from the streamer (solid line-style) and from the CHs (dashed line-style). The over-plotted diamonds highlight the LDEM values at their respective mean electron temperature T_e, while the horizontal lines indicate the temperature spread $T_e \pm W_T$ of each LDEM. While the LDEM in voxels within the streamer are typically peaked at a temperature $\gtrsim$1.3 MK, the LDEM in voxels within the CHs monotonically decrease with increasing temperature, due to the relatively dominating emissivity of the 171 Å band in that region. Indeed, in voxels of the CHs the LDEM best predicts the tomographic EUV emissivities by means of a Gaussian model with a negative centroid, as to match the progressively smaller emissivities of the 171, 193 and 211 Å bands. The Gaussian LDEM model is successful in the whole DEMT computational volume, predicting the tomographic emissivities to accuracy $\lesssim$1% in streamers and $\lesssim$10% in CHs.

The right panel of Figure 2 shows the statistical distribution of the LDEM temperature spread W_T relative to the LDEM mean temperature T_e, for all the tomographic voxels in both the streamer (solid line-style) and the CHs (dashed line-style). The ratio W_T/T_e represents the characteristic variability of the electron temperature between different spatial points within a voxel. The characteristic (median) relative temperature spread is $W_T/T_e \approx 25\%$ in voxels of the streamer and $\approx$45% in voxels of the CHs. A similar degree of relative variability is expected to characterize the distribution of electron density within each voxel, whose scale height along magnetic field lines is proportional to the electron temperature. The plots in Figure 2 correspond to CR-2223, with results for CR-2219 being virtually the same.

Comparison of synthetic images derived from models against actual data is an important validation test. For all three EUV bands, Figure 3 shows AIA images as well as synthetic ones, and their comparison. The synthetic EUV images were computed using the (either DEMT or AWSoM) 3D electron density and temperature, the instrumental passbands, and the atomic database and plasma emission model CHIANTI V9 (Del Zanna et al., 2015). The DEMT synthetic images are systematically (and significantly) more consistent with actual AIA images than the AWSoM synthetic images, as quantified by the comparative histograms. In these specific images, the East limb longitude corresponds to Carrington longitude $\approx$155°, in the center of the region where there is a larger discrepancy between the southern hemisphere O/C boundary of the AWSoM model and the DEMT density/temperature structure. It is evident that the location of the streamer/CH boundary of the images (clearly seen in both the 193 and the 211 Å bands) is faithfully reproduced by the DEMT images, while the AWSoM images show this boundary shifted to lower latitudes in the southern hemisphere. This indicates that the O/C boundary of the model is not accurate in the southern hemisphere. The location and shape of the O/C boundary of the model is highly sensitive to the specific synoptic magnetogram used as boundary condition. This discrepancy is indicating that, for these rotations, the ADAPT-GONG magnetograms are not able to reproduce the large-scale structure of the CH boundary in this specific region of the southern hemisphere.
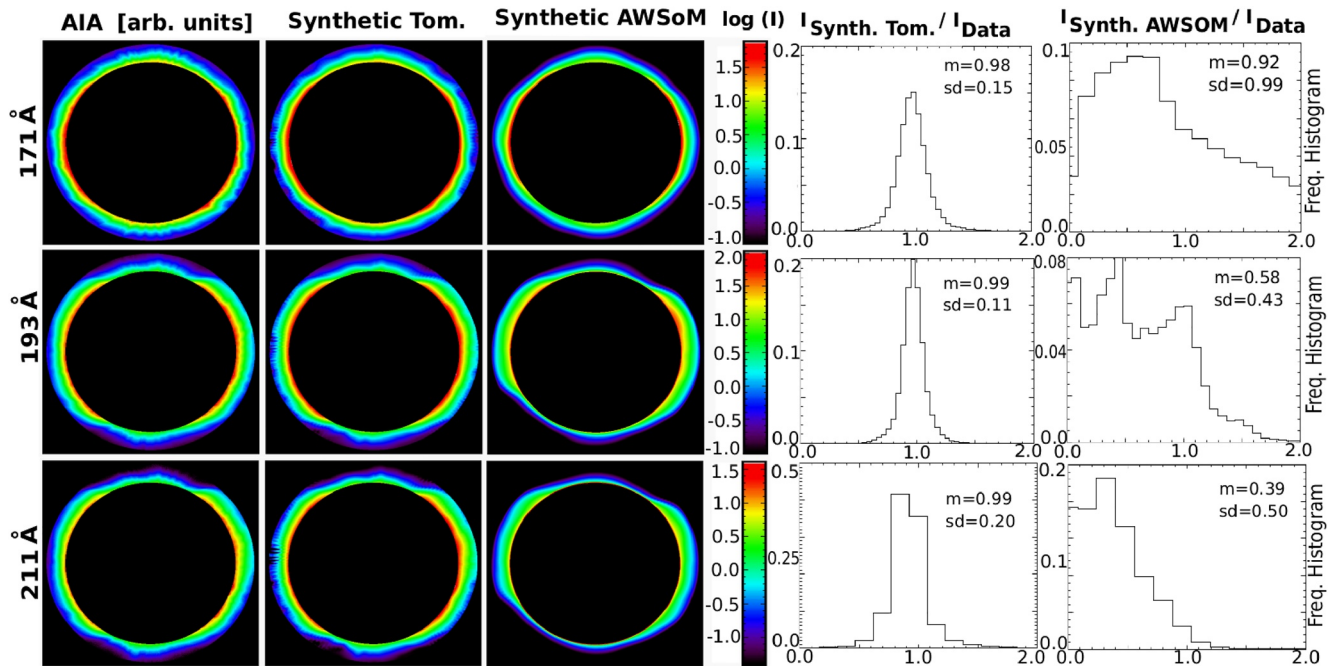
Figure 3. Comparison of actual Atmospheric Imaging Assembly (AIA) images (taken on 2019-10-25 UT 03) against synthetic ones, for bands 171, 193 and 211 Å (from tom to bottom). The images are masked (black color) outside the field-of-view radial range 1.02–1.25 $R_\odot$. From left to right: AIA image, differential emission measure tomography (DEMT) synthetic image, Alfvén Wave Solar atmosphere Model (AWSoM) synthetic image, and histograms of the pixel-by-pixel ratio I_{SYNTH}/I_{DATA} for DEMT and AWSoM, respectively.

For both rotations, DEMT and AWSoM results were traced along the magnetic field lines given by the MHD model. Figure 4 show the latitude–longitude location (at heliocentric height $r = 1.105\ R_\odot$) of the field lines for which the criteria (a)–(c) of Section 2.3 is met. Using a four-color code, type 0, I, II, and III field lines (see Table 1) are shown in blue, orange, red, and cyan color, respectively. Figure 4 shows that the streamer belt is characterized by the presence of magnetic loops of type 0 (down loops), similarly to previous DEMT studies of solar minima rotations (Nuevo et al., 2013; Lloveras et al., 2017, 2020). The MHD model is not able of
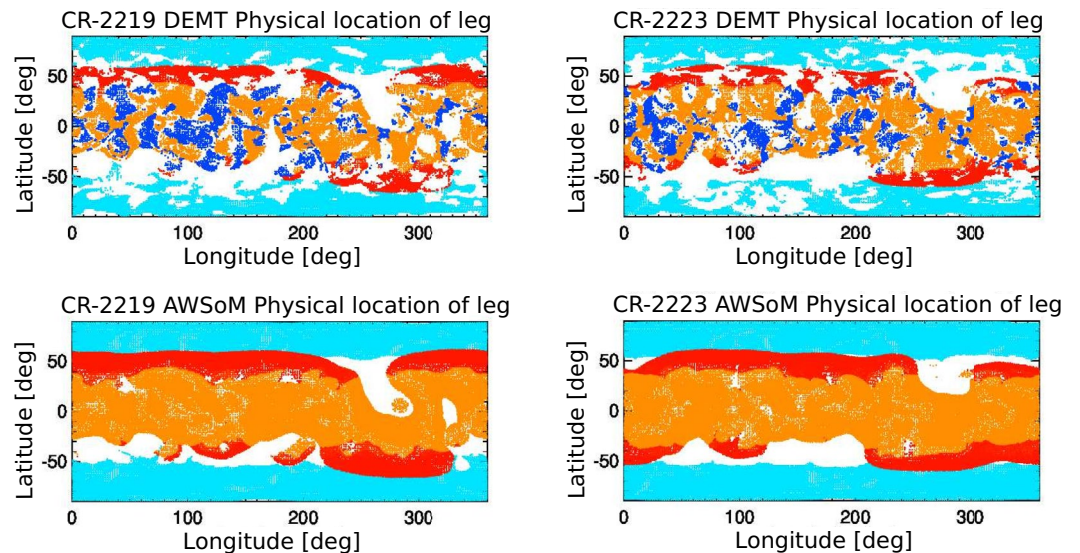

Figure 4. Latitude-longitude position of traced magnetic field lines at heliocentric height $r = 1.105\ R_\odot$ for CR-2219 (left panels) and CR-2223 (right panels), for which criteria (a), (b), and (c) of Section 2.3 are met. The location of lines of type 0, I, II, and III (see Table 1) is shown in blue, orange, red, and cyan color, respectively.
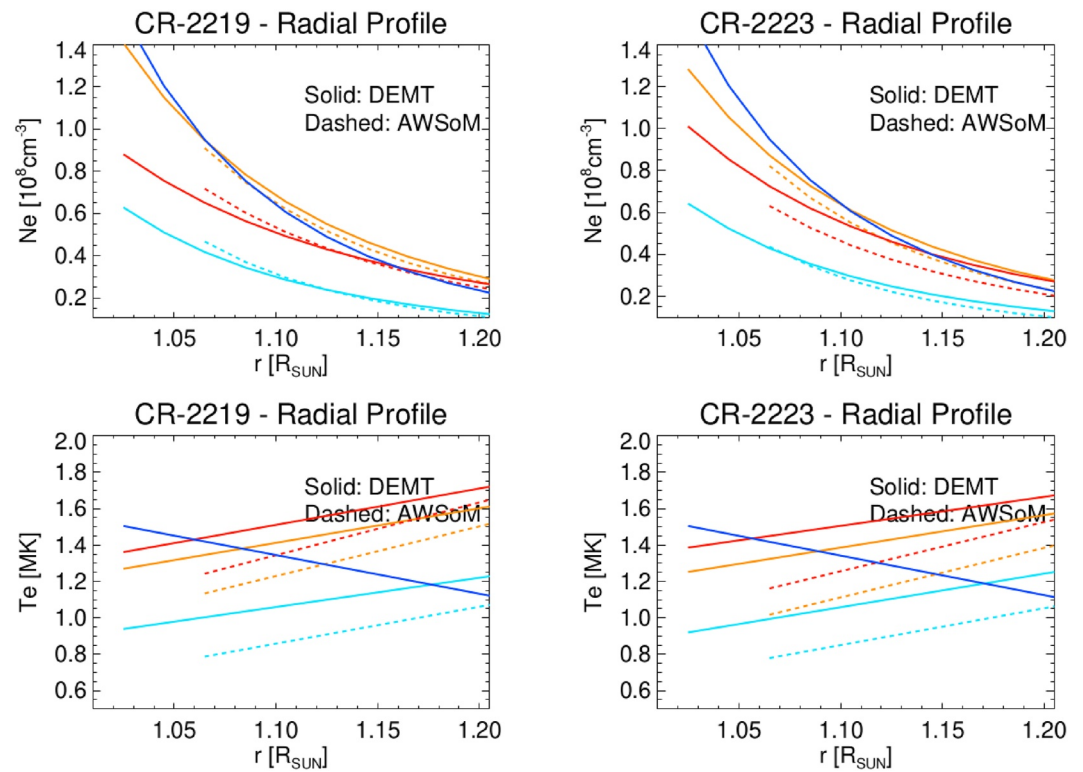
Figure 5. Average fits to $N_e(r)$ (top panels) and $T_e(r)$ (bottom panels) for field lines of type 0 (blue), I (orange), II (red), and III (cyan), for CR-2219 (left panels) and CR-2223 (right panels). Solid lines correspond to differential emission measure tomography (DEMT) results while dashed lines correspond to the Alfvén Wave Solar atmosphere Model (AWSoM) model, which does not have type 0 lines.

reproducing down loops. In these specific rotations, the fractional population of down loops is significant but smaller (about half) of what was found during rotations of the SC 23/24 deep minimum epoch, as reported by Lloveras et al. (2020).

To provide a summary of the 3D results for both rotations, Figure 5 shows the average fits to $N_e(r)$ and $T_e(r)$, as given by Equations 4 and 5, within the AIA FoV for each type of field line defined in Section 2.3, as derived from DEMT (solid lines) and the AWSoM model (dashed lines). For both rotations, the electron density results of the AWSoM model are highly consistent with tomographic reconstructions, both in terms of absolute value and scale height. Also for both rotations, the electron temperature of the AWSoM model is very consistent with the tomographic results, both in terms of absolute value and radial gradient, with the model systematically exhibiting temperature values $\approx 15\%$ smaller than the tomographic results.

For the different types of field lines, Figures 6 and 7 show the statistical distribution of results for CRs 2219 and 2223, respectively. Tomographic results are shown in solid line style and the AWSoM model results in dashed line style. The left and middle panels show the electron density at the coronal base (specifically at $r = 1.055$ R$_\odot$, where the AWSoM model reaches coronal values) and the density scale height. In a similar fashion, the right panels show the field line averaged electron temperature $\langle T_e \rangle$. These plots reveal in 3D detail the density and temperature structure of both the DEMT reconstructions and the AWSoM model, being both highly consistent in all regions. From top to bottom, the left and middle panels of Figures 6 and 7 show how the electron density at the coronal base decreases (and the scale height increases) when moving from the core region of the streamer (type 0 and I field lines) to its outer layers (type II field lines). Also, the coronal base density and scale height decrease when moving from the streamer out to the open region (type III field lines). Similarly, the right panels show how that the electron temperature increases when moving from the streamer core to its outer layers, and then decreases when moving out to the open regions. These trends are observed for both the DEMT results and the AWSoM model.
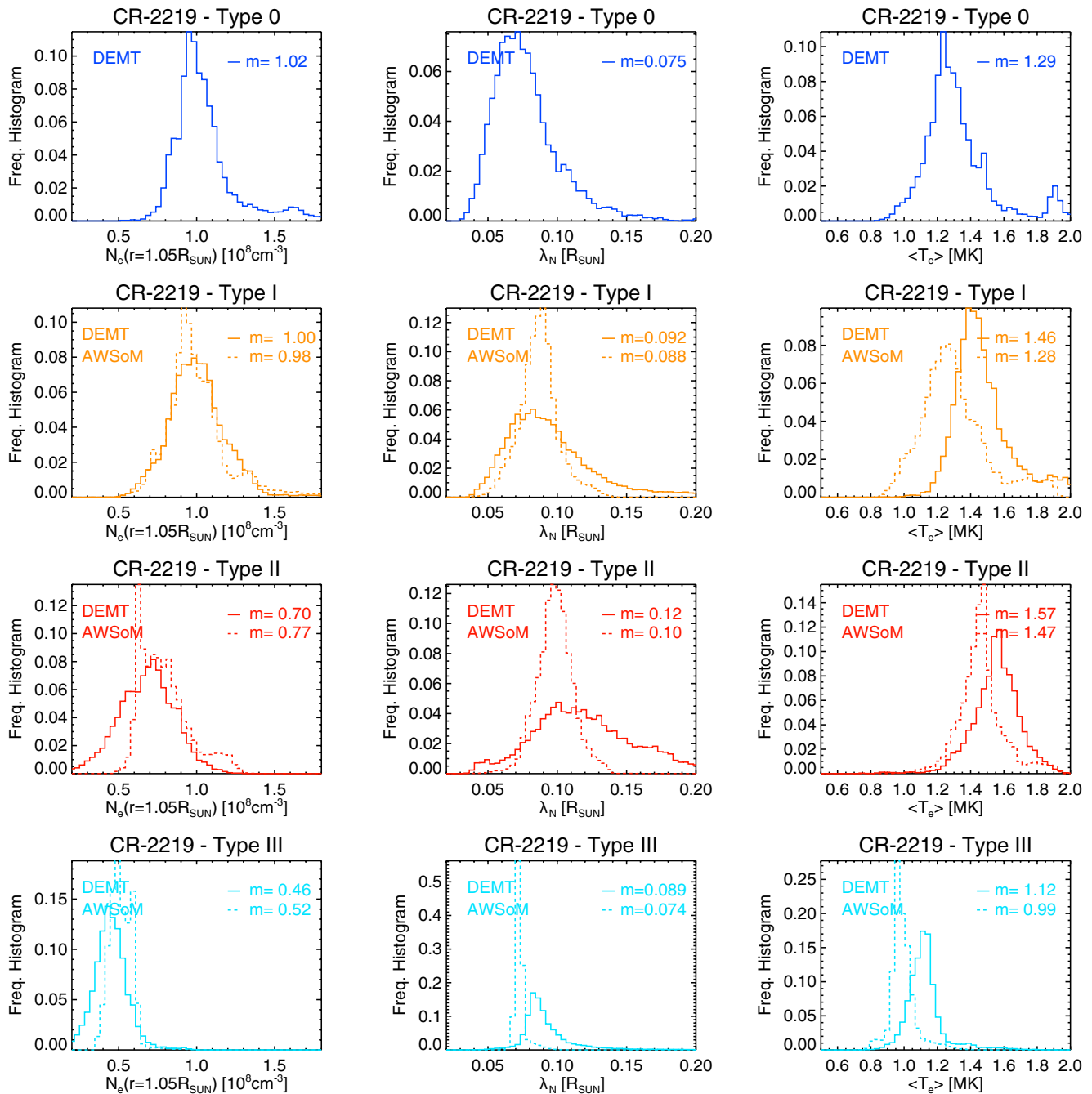
Figure 6. Statistical distribution of the results for CR-2219 from differential emission measure tomography (solid lines) and Alfvén Wave Solar atmosphere Model (AWSoM) (dashed lines) traced along magnetic field lines of type 0, I, II and III (from top to bottom and using the same color code as in Figure 5). From left to right: electron density at the lowest coronal height of the AWSoM model $N_e(r = 1.055\ R_\odot)$, electron density scale height λ_N within the Atmospheric Imaging Assembly field-of-view, and field line averaged electron temperature $\langle T_e \rangle$. In each panel the median values m are indicated.

Table 2 summarizes a quantitative comparative analysis between the results of the AWSoM model and the DEMT reconstructions. Error bars of the DEMT products due to their dominating sources of uncertainty (radiometric calibration and tomographic regularization) were determined by Nuevo et al. (2015) and Lloveras et al. (2017). Statistically, the electron density at the coronal base of the AWSoM model matches the reconstructed values within $\approx 1 - 13\%$ accuracy (depending on the specific region and rotation), a difference comparable to the DEMT uncertainty level $\Delta N_{CB} \approx 10\%$. Similarly, the density scale height of the AWSoM model is systematically smaller than the tomographic result within $\approx 4 - 19\%$ accuracy, differences well beyond the DEMT uncertainty level
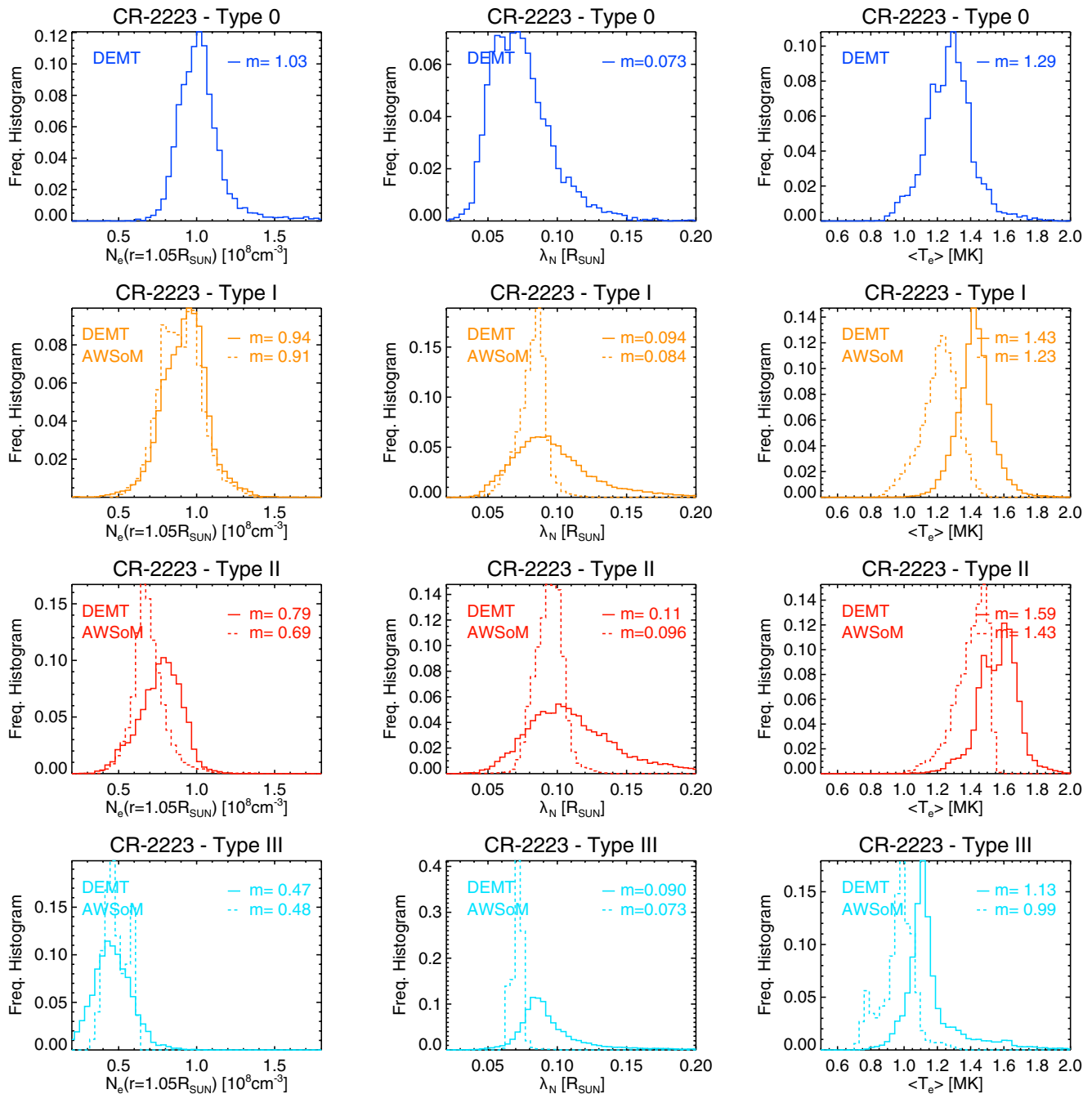
Figure 7. Same as Figure 6 for CR-2223.

$\Delta\lambda_N \approx 2\%$. Also, the temperature of the AWSoM model is systematically smaller than the tomographic result within $\approx 6 - 14\%$ accuracy, a difference comparable or larger than the uncertainty in the DEMT temperature $\Delta T_e \approx 5\%$.

As a closing remark, it is interesting to quantify the degree of departure of DEMT results for electron density and temperature from the values expected for an isothermal hydrostatic plasma. For such a regime, the values of λ_N listed in Table 2 imply electron temperature values that differ from the corresponding listed values of $\langle T_e \rangle$ by 5%–20%, with the larger departure corresponding the open field region. These differences are relatively small, which is expected at the low heights analyzed by DEMT ($r < 1.25\ R_\odot$), where the wind speed is either negligible (closed region) or rather small (open regions), as analyzed in detail by Lloveras et al. (2017).

Table 2

Median Value (Indicated as "Md") of the Statistical Distribution of $N_{CB} \equiv N_e(r = 1.055\ R_\odot)$, λ_N, and $\langle T_e \rangle$ Shown in Figures 6 and 7

Type	Md(N_{CB}) [10^8 cm^{-3}]	Md(λ_N) [$R_\odot$]	Md ($\langle T_e \rangle$) [MK]
CR-2219			
0	1.02	0.075	1.29
I	1.00 (−2%)	0.092 (−4%)	1.46 (−12%)
II	0.70 (+1%)	0.120 (−17%)	1.57 (−6%)
III	0.46 (+13%)	0.089 (−17%)	1.12 (−12%)
CR-2223			
0	1.03	0.073	1.29
I	0.94 (−3%)	0.094 (−11%)	1.43 (−14%)
II	0.79 (−13%)	0.110 (−13%)	1.59 (−10%)
III	0.47 (+2%)	0.090 (−19%)	1.13 (−12%)

Note. DEMT values are expressed in absolute terms, while AWSoM results are expressed relative to the corresponding DEMT value.

3.2. C2-SRT Reconstructions and the AWSoM Model

For CRs 2219 and 2223, Figure 8 shows latitude-longitude maps of the electron density N_e of both the C2-SRT analysis and the AWSoM model. Maps are shown at a sample heliocentric height $r = 2.5\ R_\odot$, the lowest height of the LASCO-C2 radial FoV. For both rotations, there is an overall good consistency between the AWSoM and the C2-SRT maps, both in terms of shape and size of the streamer belt and the CHs, as well as in terms of characteristic values and their dynamic range. The AWSoM model exhibits density values systematically somewhat larger than the tomographic results, as detailed below. The location and shape of the O/C boundaries of the AWSoM model reasonably match the transition of the C2-SRT N_e from larger values in the streamer belt (red/yellow colors) to smaller CHs values (green/blue colors).

As in the previous section, comparison between synthetic images (derived from either C2-SRT or AWSoM) against actual data, constitutes a good validation test for both the reconstruction and the model. Figure 9 shows an example of a LASCO-C2 image as well as synthetic ones, and their comparison. C2-SRT images are again systematically more consistent with the actual LASCO-C2 images than the AWSoM synthetic images, as quantified by the comparative histograms. As an example of comparison of smaller-scale features among these images, note that in this specific case the East limb of the LASCO-C2 image, which corresponds to Carrington longitude ≈270°, shows a doubled peaked streamer. This feature is more faithfully reproduced by the C2-SRT synthetic image, while the AWSoM synthetic image shows only one peak.

For both rotations, C2-SRT and AWSoM results were traced along magnetic open field lines given by the MHD model, in the range of heights covered by the LASCO-C2 FoV. To provide a summary of the 3D results for both rotations, Figure 10 shows the average power law fits to $N_e(r)$, as given by Equation 6, for the open field lines traced in the northern hemisphere (red color) and the southern one (blue color) separately. The C2-SRT results are plotted in solid line style and the AWSoM model results in dashed line style. For both rotations is evident
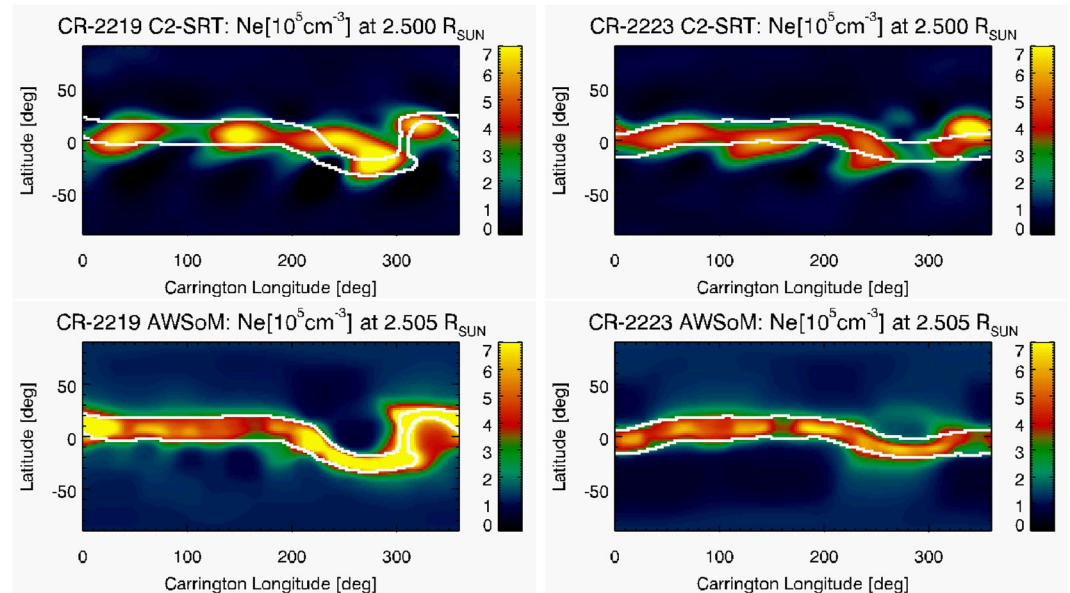

Figure 8. Latitude-longitude maps of electron density N_e for CR-2219 (left panels) and CR-2223 (right panels) at the heliocentric height $r = 2.5\ R_\odot$, from Large Angle and Spectrometric COronagraph-C2 tomography (C2-SRT, top panels) and from the Alfvén Wave Solar atmosphere Model (AWSoM) model (bottom panels). In each panel, the over plotted thick-white curves indicate the open/closed boundaries according to the AWSoM model.
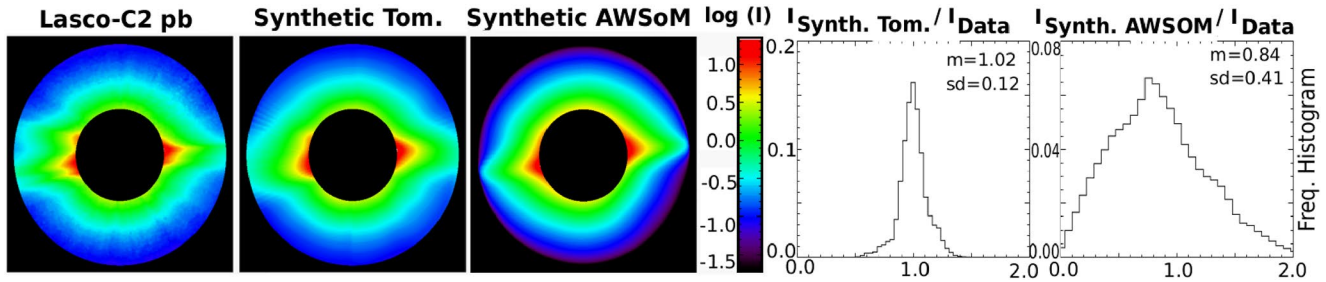
Figure 9. Comparison of an actual Large Angle and Spectrometric COronagraph (LASCO-C2) image (taken on 2019-10-16 UT 09) against synthetic ones. The images are masked (black color) outside the field-of-view radial range 2.5–6.0 $R_\odot$. From left to right: LASCO-C2 pB-image, C2-solar rotational tomography (SRT) synthetic image, Alfvén Wave Solar atmosphere Model (AWSoM) synthetic image, and histograms of the pixel-by-pixel ratio I_{SYNTH}/I_{DATA} for C2-SRT and AWSoM, respectively.

that, compared to the tomographic results, the AWSoM model overestimates the electron density values in both hemispheres, as well as underestimates its scale height.

Figures 11 and 12 show the statistical distribution of results for CRs 2219 and 2223, respectively. Tomographic results are shown in solid line style and the AWSoM model results in dashed line style, with red curves indicating results for the northern hemisphere and blue curves corresponding to the southern hemisphere. Left panels show the electron density at the lowest height of the LASCO-C2 FoV, that is, $N_e(r = 2.5\ R_\odot)$, while right panels show the height-averaged density scale height $\langle\lambda_N\rangle$ of the fit, as indicated by Equation 7.

Table 3 summarizes a quantitative comparative analysis between the AWSoM model and the results of C2-SRT reconstructions. The uncertainty level of C2 pB values is estimated to be $\approx$15% (Frazin et al., 2012; Lamy et al., 2020). The uncertainty in the electron density introduced by the tomographic reconstruction is $\approx$10%, estimated from the spread of the I_{SYNTH}/I_{DATA} histogram for C2-SRT shown in Figure 9. Considering those estimates, the uncertainty of the electron density from the C2-SRT is $\Delta N_e \approx 20$%, which implies for the scale height of the fitted power-law an uncertainty $\Delta\langle\lambda_N\rangle \approx 15$%. In both rotations the electron density of the AWSoM model at height 2.5 $R_\odot$ is $\approx$20–75% larger than that of the reconstruction (depending on the hemisphere and rotation), differences that are 2–3 times the uncertainty level of the C2-SRT electron density. The density scale height of the model is 10–20% smaller than that of the reconstruction, a difference that is comparable to the uncertainty of the C2-SRT scale height.

As a closing remark, from the median value of the histograms of the height-averaged scale height $\langle\lambda_N\rangle$, and Equation 7, the characteristic values of the exponent of the power law fits are $\approx$2.8 and $\approx$3.3 for the C2-SRT reconstructions and the AWSoM model, respectively. Finally, we also highlight that the characteristic values of λ_N from the C2-SRT analysis are far from consistent with a isothermal hydrostatic regime, for which $\lambda_N \approx 1.5\ R_\odot$ implies $T_e \approx 22$ MK, a clearly non-physical result in these coronal structures. It is expected that the solar wind electron density could not be approximated well by the hydrostatic regime approximation over the LASCO-C2 radial FoV, 2.5–6.0 $R_\odot$, as anticipated in Sec. 2.3 in discussing the power law in Equation 6.
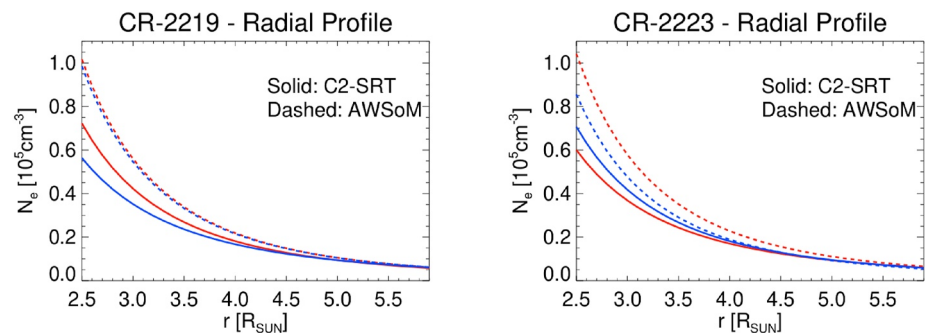

Figure 10. Average power law fits to $N_e(r)$ along open field lines traced in the northern CH (red) and the southern CH (blue) for CR-2219 (left panel) and CR-2223 (right panel). Solid lines correspond to C2-solar rotational tomography (SRT) results while dashed lines correspond to the Alfvén Wave Solar atmosphere Model (AWSoM) model.
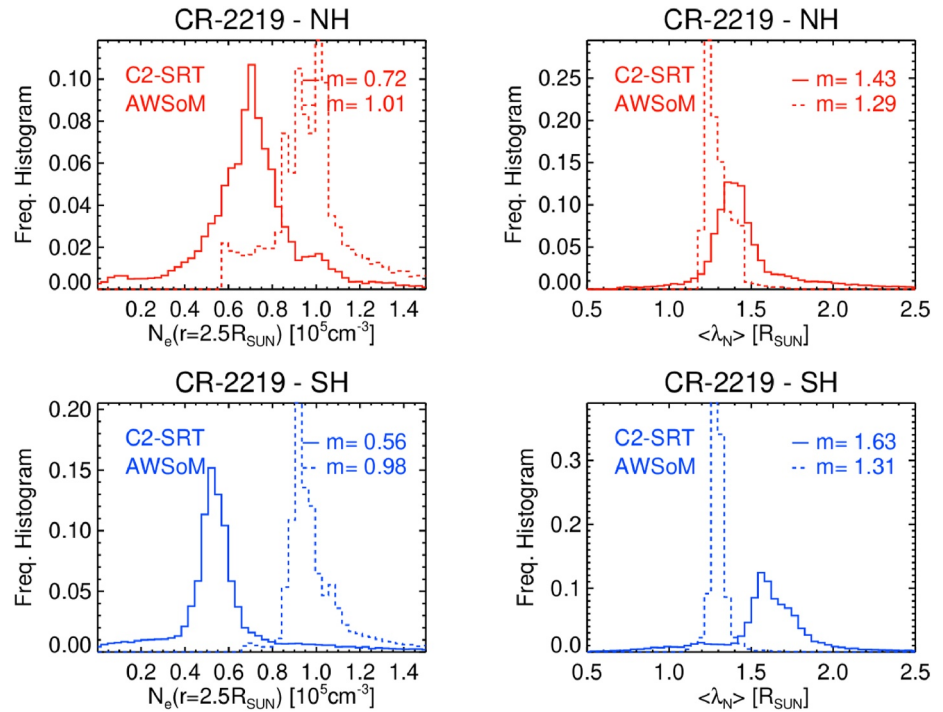
Figure 11. Statistical distribution of the results for CR-2219 from C2-solar rotational tomography (SRT) (solid lines) and Alfvén Wave Solar atmosphere Model (AWSoM) (dashed lines) traced along open field lines of the northern hemisphere (NH, top panels and red color) and the southern hemisphere (SH, bottom panels and blue color). The left panels show the electron density at the lowest heliocentric height of the Large Angle and Spectrometric COronagraph (LASCO-C2) field-of-view (FoV) $N_e(r = 2.5\ R_\odot)$, while the right panels show the electron density scale height $\langle\lambda_N\rangle$, height-averaged over the LASCO-C2 radial FoV. In each panel the median values m are indicated.
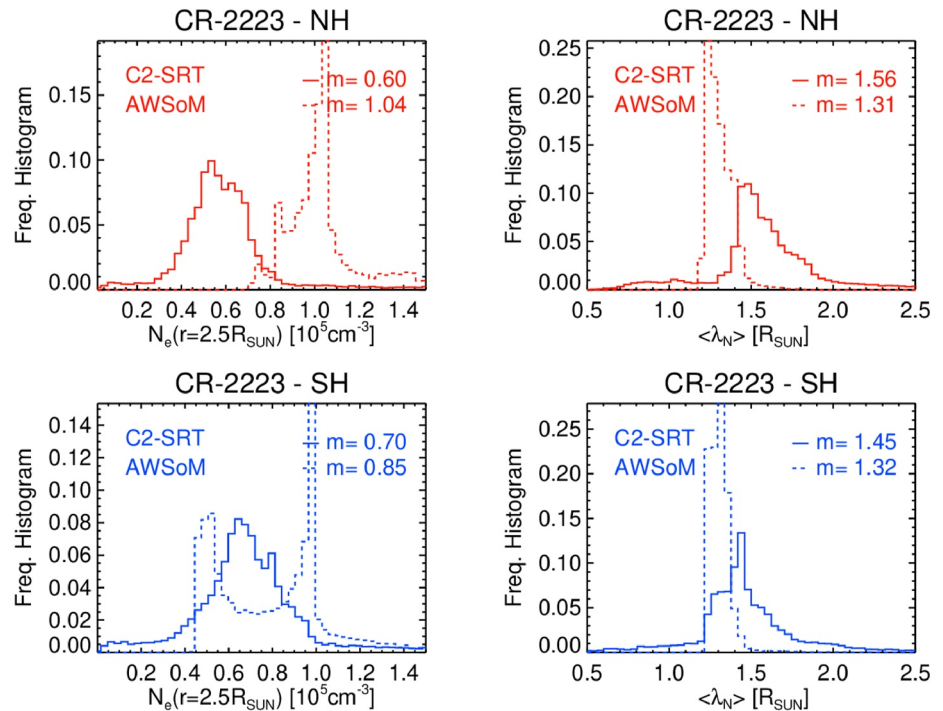

Figure 12. Same as Figure 11 for CR-2223.

Table 3
Median Value (Indicated as "Md") of the Statistical Distribution of $N_e(r = 2.5 R_\odot)$ and $\langle\lambda_N\rangle$ Shown in Figures 11 and 12

Type	Md(N_e) [10^5 cm^{-3}]	Md($\langle\lambda_N\rangle$) [$R_\odot$]
CR-2219		
NH	0.72 (+40%)	1.43 (−10%)
SH	0.56 (+75%)	1.63 (−20%)
CR-2223		
NH	0.60 (+73%)	1.56 (−16%)
SH	0.70 (+21%)	1.45 (−9%)

Note. NH, northern hemisphere; SH, southern hemisphere. C2-SRT values are expressed in absolute terms, while AWSoM results are expressed relative to the corresponding C2-SRT value.

3.3. Terminal Wind Speed and DEMT Results

The correlation between the terminal wind speed of the AWSoM model and the electron density and temperature of the low corona as derived from DEMT was investigated. Open field lines were traced from the coronal base up to a maximum height $r_M = 20$ R$_\odot$, where the model essentially reached its terminal properties. In order to evenly thread the volume of the open region, $N = 90 \times 180 = 16,200$ starting points were uniformly set in longitude and latitude (with a 2° spacing) at an intermediate heliocentric height of $r_0 = 6$ R$_\odot$, where closed field lines of the model are essentially absent. For each of the N starting points, the field line passing through that location was traced both inwards down to the coronal base as well as outwards up to r_M. For each traced field line, the DEMT field line averaged electron temperature $\langle T_e \rangle$ and the coronal base electron density $N_e(r = 1.05$ R$_\odot)$ were determined, as well as the AWSoM model terminal wind speed $V_r(r_M)$.

As shown by Figure 1, some open field lines of the model thread locations where the DEMT electron density is characteristic of the streamer belt region. As shown by the analysis of Figure 3, this discrepancy is most probably due to lack of accuracy of the ADAPT-GONG maps, and the DEMT electron density results at the coronal base can be used as a proxy to discern locations that belong to the streamer belt from those within the CHs. As in the previous sections, only field lines of type III were selected for analysis, as those are the ones which effectively thread CH regions according to the DEMT reconstructions.

The top panels of Figure 13 show latitude-longitude maps of the AWSoM model radial solar wind speed $V_r(r_M)$ for all selected open field lines, where the white regions correspond to non-selected field lines. For all field lines indicated in the top panels, middle panels show the scatter plots of the DEMT coronal base electron density $N_e(r = 1.05$ R$_\odot)$ versus the terminal radial wind speed $V_r(r_M)$ signed by B_r (i.e., multiplied by Sgn(B_r)) to separate results of the Northern and Southern hemispheres as positive and negative values, respectively. Similarly, the bottom panels show the scatter plots of the DEMT field line averaged electron temperature $\langle T_e \rangle$ versus Sg(B_r) $V_r(r_M)$. In middle and bottom panels the straight lines indicate the best Theil-Sen linear fit to the data in each hemisphere. The data points in the scatter plots are colored by the absolute value of the latitude of the field line at r_M.

These plots show that the model field lines threading the CHs exhibit a mean trend of anti-correlation between their terminal wind speed and both the DEMT electron density near the coronal base and the characteristic (field line averaged) DEMT electron temperature, for for both hemispheres of the two analyzed rotations. The vertical spread of the data points around the observed trends (both for the density and temperature plots) is in the range ≈25–45%, depending on the rotation and hemisphere. This is consistent with the characteristic LDEM temperature spread W_T within each voxel, which as discussed in relation to Figure 2 is ≈45% in CHs. Note also that slower terminal speeds tend to be found along field lines that terminate at lower latitudes, near the heliospheric current sheet (HCS), whose shape and location is bounded by the white contours in Figure 8. On the other hand, in general, the larger the terminal wind speed the larger the terminal latitude of the field line, except for localized regions (exhibiting the largest terminal speeds) in the Northern hemisphere of CR-2219 and the Southern hemisphere of CR-2223.

4. Discussion and Conclusions

The 3D thermodynamic structure of the global corona was studied for two WHPI campaign periods, CRs 2219 and 2223. Tomographic reconstructions of the electron density and temperature were carried out using EUV and WL images. Also, steady-state 3D MHD simulations of the two rotations were computed using the AWSoM model and compared in detail with the reconstructions.

The DEMT reconstructions, which use AIA/SDO images, cover the range of heliocentric distance 1.02–1.25 R$_\odot$, and their results are quantitatively summarized in Table 2. For both rotations, the DEMT analysis shows that progressively outer layers of the equatorial streamer belt exhibit decreasing coronal base density, increasing density scale height, and increasing electron temperature. In transitioning from the closed region of the streamer
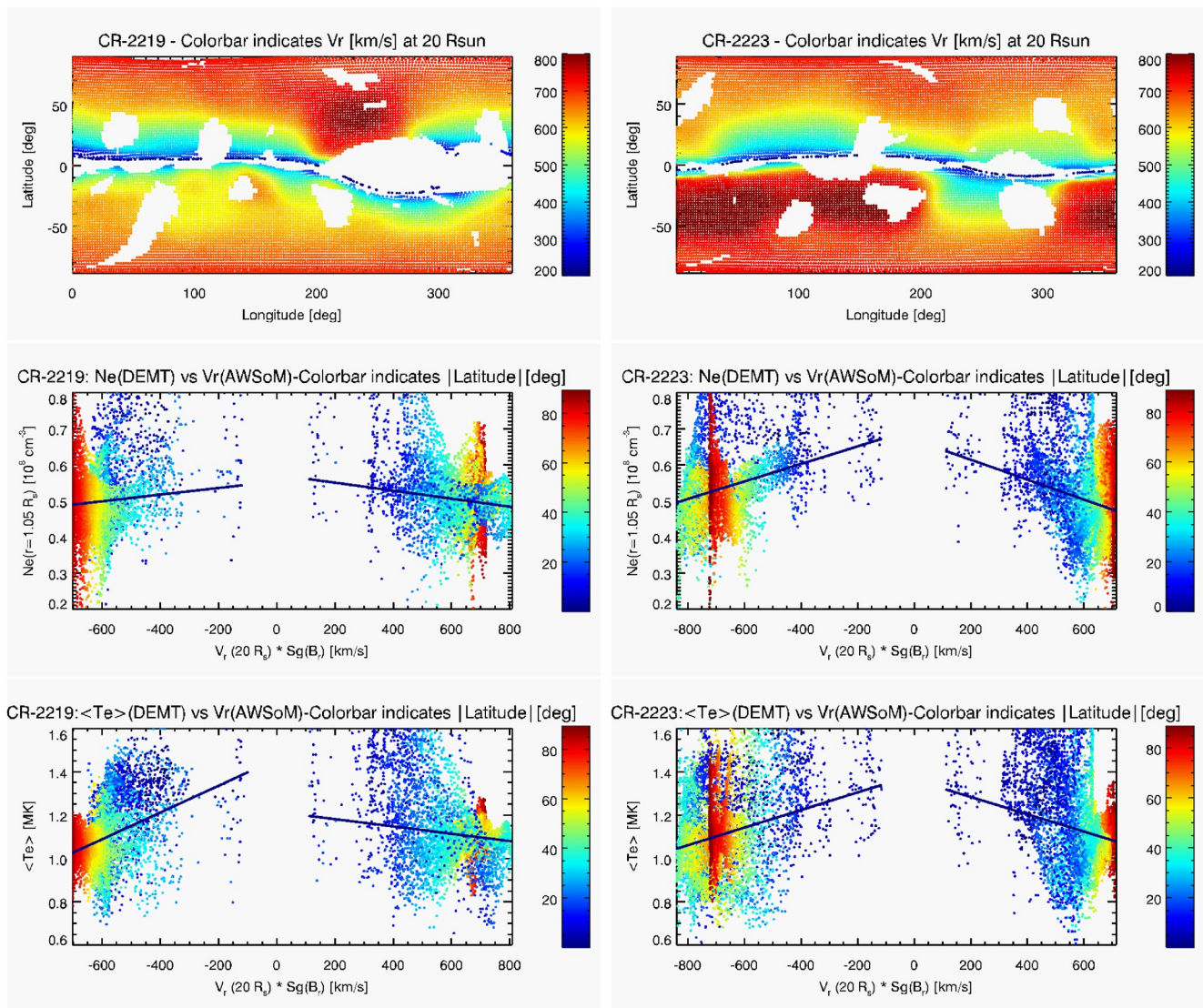
Figure 13. Top panels: latitude-longitude maps of the radial component of the Alfvén Wave Solar atmosphere Model (AWSoM) model terminal solar wind speed $V_r(r_M = 20\ R_\odot)$ [km s^{-1}], for CR-2219 (left panel) and CR-2223 (right panel), where each dot corresponds to a traced open field line that effectively threads a CH according to the differential emission measure tomography (DEMT) reconstructions (see text in Section 3.3). Middle panels: scatter plots of the DEMT coronal base density $N_e(r = 1.05\ R_\odot)$ versus the AWSoM model terminal wind speed $V_r(r_M)$ signed by B_r (i.e., multiplied by $\mathrm{Sgn}(B_r)$), for all field lines indicated in the top panels. Abscissa negative values correspond to the southern hemisphere and positive ones to the northern hemisphere. Bottom panels: scatter plots of the DEMT field line averaged electron temperature $\langle T_e \rangle$ versus $\mathrm{Sg}(B_r)\ V_r(r_M)$, for the same field lines. In the middle an bottom panels, straight lines indicate the best Theil-Sen estimator linear fit to the data in each hemisphere. The colorbars indicate the module of the heliocentric latitude of the field line at heliocentric height r_M.

out to the open regions of the CHs, the electron density at the coronal base and its scale height decrease, as well as the electron temperature. These trends are all in accordance with previous DEMT studies (Lloveras et al., 2017, 2020) that analyzed CRs 2081 and 2082, during the SC 23/24 deep minimum epoch. Compared to those rotations, the WHPI targets exhibit $a \approx 20\%$ lower coronal base density, $a \approx 20\%$ larger scale height and $a \approx 20\%$ larger electron temperature. Also, for both WHPI rotations the overall O/C structure of the AWSoM model agrees quite well with the density and temperature structure of DEMT reconstructions, except between Carrington longitudes ≈ 0–200° in the southern hemisphere, where the match is poorer. Comparison of synthetic images, computed from the DEMT reconstructions and from the AWSoM model, against actual AIA data shows that those derived from tomography are significantly (and systematically) a better match, strongly suggesting that the adapt-GONG maps (here used as boundary conditions for AWSoM) are not accurate in the mismatch region. Quantitative comparison of the AWSoM model against the DEMT reconstructions shows that the electron density

at the coronal base agree with the tomographic results within their ≈10% uncertainty. The scale height and electron temperature of the model are systematically ≈5–20% smaller than the reconstructed values (depending on the rotation and coronal region), differences up to fourfold their ≲5% uncertainty.

While quite successful matching the large-scale structure of the DEMT reconstructions, the AWSoM model (used in its latest version for this study) does not reproduce small-scale coronal features systematically revealed by DEMT. First, loops with temperature decreasing with height (known as "down loops") were found in the low latitudes within the streamer belt, as in previous DEMT solar minima studies (Huang et al., 2012; Lloveras et al., 2017, 2020; Nuevo et al., 2013). Such structures are expected where heating is strongly enhanced at the coronal base. This has been explored by Schiff and Cranmer (2016), who used a 1D model to simulate down loops by including coronal heating dissipation of compressive waves formed by mode conversion from an initial population of Alfvén waves, a physical mechanism originally proposed by Nuevo et al. (2013). Second, as in previous DEMT studies, the reconstructions reveal that the coronal plasma is ubiquitously characterized by a significant local temperature spread within the $\sim10^4$ km linear size of the tomography computational cell (Vásquez, 2016). As shown in this study, the characteristic temperature spread of the LDEM (characterizing the temperature distribution of the plasma within an individual cell) is found to be ≈25% in streamers and ≈45% in CHs. Furthermore, streamers also exhibit multi-modal LDEM, resulting in even larger temperature dispersion within the tomographic cell's spatial scale (Nuevo et al., 2015). Except across specific localized regions, such as the O/C boundaries, 3D-MHD models such as as AWSoM do not exhibit such fine structure (Shi et al., 2022). The LDEM is a measure of the temperature distribution across a large number of thermally isolated magnetic flux tubes threading any given individual tomographic cell. Its spread implies a similar degree of fine structure in the density within the cell, so that significant Alfvén speed gradients perpendicular to the field direction can be expected within that same spatial scale. We speculate that taking into account this level of fine-structure by global 3D-MHD models may be significantly consequential for their predictions on dynamics of phenomena in the solar corona, such as Alfvén wave propagation.

The WL-SRT reconstructions, wich use SoHO/LASCO-C2 *pB* images, cover the range of heliocentric distance 2.5–6.0 R$_\odot$, and their results are quantitatively summarized in Table 3. For the two rotations analyzed in this work, the reconstructed electron density exhibits similar values and trends with height as those found in WL tomographic reconstructions and global models of rotations selected from the SC 23/24 minimum epoch (Morgan & Cook, 2020; Sachdeva et al., 2019; Vibert et al., 2016; Wang et al., 2017). Quantitative comparison of the AWSoM model against the C2-SRT reconstructions shows that the electron density of the model is 20–75% larger (depending on the hemisphere and rotation) than the reconstructed values at the inner boundary of the LASCO-C2 radial FoV, a difference up to threefold their uncertainty. Also, within the C2 FoV, the scale height of the electron density of the model is systematically 10–20% smaller than the reconstructed values, a difference comparable to their ≈15% uncertainty. Synthetic images computed from C2-SRT reconstructions compare to actual LASCO-C2 data significantly better than those computed from the AWSoM model, strongly suggesting that the model overestimates the electron density in the FoV of LASCO-C2 by up to 75%. This is likely due to the acceleration of the model being more gradual and extended (with acceleration up to 15 R$_\odot$ or more) than what is observed in large coronal holes. Future planned enhancements of the AWSoM model include a multi-fluid description and improvement of the energy cascading process, which can both significantly affect the heating and acceleration of the solar wind model. In addition, we will include model validation from various observational data products including tomography.

We conclude discussing the results of the joint analysis of the DEMT reconstructions and the solar wind velocity field of the AWSoM model. For both hemispheres of the two analyzed rotations, model's field lines were traced threading the whole volume of the CHs. It is found that the model's terminal wind speed along field lines is anti-correlated with their DEMT reconstructed values of density and temperature at the low corona. It is also found that the terminal latitude of the field lines tends to be larger for larger terminal speeds, with the exception of specific localized regions of very high speed streams. This analysis constitutes an interesting 3D validation of the AWSoM wind model, showing that its slow component is associated with field lines that exhibit larger electron density and temperature near the streamer brightness boundary, forming the so called "streamer's legs" (Suess et al., 2009), that terminate near the HCS. On the other hand, the fast component of the wind model is found to be associated with open field lines exhibiting relatively lower values of DEMT density and temperature, and terminating at larger latitudes, deeper into the CHs. These results are consistent with the scenario in which,

during solar minima, the slow solar wind originates along open field lines closest to the streamer belt while the fast wind originates from the CHs (Y. M. Wang & Sheeley, 1990).

This work is the third one of a series of tomographic studies aiming at characterizing in 3D detail the global structure of the corona during the last three minima of solar activity (Lloveras et al., 2017, 2020). In the context of the two specific WHPI periods chosen for study, this work also demonstrates the value of tomographic reconstructions for validation of 3D-MHD models. As new space borne and ground based solar telescopes are coming into operation, further opportunities for development and application of tomographic techniques will arise. Future projects will involve analysis of rotations selected from epochs different than minima, over the current and previous SCs.

Data Availability Statement

The 3D tomographic reconstructions and 3D magneto-hydrodynamic simulations of the solar corona and solar wind of Whole Heliosphere and Planetary Interactions targets CR-2219 and CR-2223 used in the article are available at zenodo.org via https://doi.org/10.5281/zenodo.6470700 (Lloveras et al., 2022).

References

Altschuler, M. D., & Perry, R. M. (1972). On determining the electron density distribution of the solar corona from K-coronameter data. *Solar Physics*, *23*(2), 410–428. https://doi.org/10.1007/BF00148104

Arge, C. N., Henney, C. J., Hernandez, I. G., Toussaint, W. A., Koller, J., & Godinez, H. C. (2013). Modeling the corona and solar wind using ADAPT maps that include far-side observations. In *AIP conference proceedings* (Vol. 1539, pp. 11–14). https://doi.org/10.1063/1.4810977

Bisi, M. M., Thompson, B. J., Emery, B. A., Gibson, S. E., Leibacher, J., & van Driel-Gesztelyi, L. (2011). The Sun-Earth connection near solar minimum: Placing it into context. *Solar Physics*, *274*(1–2), 1–3. https://doi.org/10.1007/s11207-011-9915-2

Butala, M. D., Hewett, R. J., Frazin, R. A., & Kamalabadi, F. (2010). Dynamic three-dimensional tomography of the solar corona. *Solar Physics*, *262*(2), 495–509. https://doi.org/10.1007/s11207-010-9536-1

Cairns, I. H., Lobzin, V. V., Warmuth, A., Li, B., Robinson, P. A., & Mann, G. (2009). Direct radio probing and interpretation of the Sun's plasma density profile. *The Astrophysical Journal Letters*, *706*(2), L265–L269. https://doi.org/10.1088/0004-637X/706/2/L265

Del Zanna, G., Dere, K. P., Young, P. R., Landi, E., & Mason, H. E. (2015). CHIANTI—an atomic database for emission lines. Version 8. *Astronomy & Astrophysics*, *582*, A56. https://doi.org/10.1051/0004-6361/201526827

Frazin, R. A., & Janzen, P. (2002). Tomography of the solar corona. II. Robust, regularized, positive estimation of the three-dimensional electron density distribution from LASCO-C2 polarized white-light images. *The Astrophysical Journal*, *570*(1), 408–422. https://doi.org/10.1086/339572

Frazin, R. A., Vásquez, A. M., & Kamalabadi, F. (2009). Quantitative, three-dimensional analysis of the global corona with multi-spacecraft differential emission measure tomography. *The Astrophysical Journal*, *701*(1), 547–560. https://doi.org/10.1088/0004-637X/701/1/547

Frazin, R. A., Vásquez, A. M., Thompson, W. T., Hewett, R. J., Lamy, P., Llebaria, A., et al. (2012). Intercomparison of the LASCO-C2, SECCHI-COR1, SECCHI-COR2, and Mk4 Coronagraphs. *Solar Physics*, *280*(1), 273–293. https://doi.org/10.1007/s11207-012-0028-3

Galvin, A. B., & Kohl, J. L. (1999). Whole Sun Month at solar minimum: An introduction. *Journal of Geophysical Research*, *104*(A5), 9673–9678. https://doi.org/10.1029/1999JA900008

Guhathakurta, M., Holzer, T. E., & MacQueen, R. M. (1996). The large-scale density structure of the solar corona and the heliospheric current sheet. *The Astrophysical Journal*, *458*, 817. https://doi.org/10.1086/176860

Harding, J. C., Cairns, I. H., & Lobzin, V. V. (2019). Offset Power-law Dependence of the Sun's Radial Electron Density Profile: Evidence and Implications. *The Astrophysical Journal*, *877*(1), 25. https://doi.org/10.3847/1538-4357/ab19a0

Huang, Z., Frazin, R. A., Landi, E., Manchester, W. B., Vásquez, A. M., & Gombosi, T. I. (2012). Newly discovered global temperature structures in the quiet sun at solar minimum. *The Astrophysical Journal*, *755*(2), 86. https://doi.org/10.1088/0004-637X/755/2/86

Jin, M., Manchester, W. B., van der Holst, B., Oran, R., Sokolov, I., Toth, G., et al. (2012). Simulate the coronal mass ejection on 2011 March 7 from chromosphere to 1 AU, In *AGU fall meeting abstracts* (Vol. 2012, p. SH33E-04).

Kalman, R. E. (1960). A new approach to linear filtering and prediction problems. *Journal of Basic Engineering*, *82*(1), 35–45. https://doi.org/10.1115/1.3662552

Kohl, J. L., Noci, G., Antonucci, E., Tondello, G., Huber, M. C. E., Cranmer, S. R., et al. (1998). UVCS/SOHO empirical determinations of anisotropic velocity distributions in the solar corona. *The Astrophysical Journal Letters*, *501*(1), L127–L131. https://doi.org/10.1086/311434

Lamy, P., Floyd, O., Mikić, Z., & Riley, P. (2019). Validation of MHD Model Predictions of the Corona with LASCO-C2 Polarized Brightness Images. *Solar Physics*, *294*(11), 162. https://doi.org/10.1007/s11207-019-1549-9

Lamy, P., Llebaria, A., Boclet, B., Gilardy, H., Burtin, M., & Floyd, O. (2020). Coronal photopolarimetry with the LASCO-C2 coronagraph over 24 years [1996–2019]. *Solar Physics*, *295*(7), 89. https://doi.org/10.1007/s11207-020-01650-y

Lloveras, D. G., Vásquez, A. M., & Nuevo, F. A. (2022). Data cubes corresponding to the article "Three-dimensional Structure of the Corona during WHPI Campaign Rotations CR-2219 and CR-2223". Zenodo, [dataset]. https://doi.org/10.5281/zenodo.6470700

Lloveras, D. G., Vásquez, A. M., Nuevo, F. A., & Frazin, R. A. (2017). Comparative study of the three-dimensional thermodynamical structure of the inner corona of solar minimum Carrington rotations 1915 and 2081. *Solar Physics*, *292*(10), 153. https://doi.org/10.1007/s11207-017-1179-z

Lloveras, D. G., Vásquez, A. M., Nuevo, F. A., Mac Cormack, C., Sachdeva, N., Manchester, W., et al. (2020). Thermodynamic structure of the solar corona: Tomographic reconstructions and MHD modeling. *Solar Physics*, *295*(6), 76. https://doi.org/10.1007/s11207-020-01641-z

Lobzin, V. V., Cairns, I. H., & Robinson, P. A. (2008). Evidence for wind-like regions, acceleration of shocks in the deep corona, and relevance of 1/f dynamic spectra to coronal type II bursts. *The Astrophysical Journal Letters*, *677*(2), L129–L132. https://doi.org/10.1086/587980

Morgan, H. (2019). An Atlas of Coronal Electron Density at 5R ⊙ II. A Spherical Harmonic Method for Density Reconstruction. *The Astrophysical Journal Supplement Series*, *242*(1), 3. https://doi.org/10.3847/1538-4365/ab125d

Morgan, H., & Cook, A. C. (2020). The width, density, and outflow of solar coronal streamers. *The Astrophysical Journal*, *893*(1), 57. https://doi.org/10.3847/1538-4357/ab7e32

Nuevo, F. A., Huang, Z., Frazin, R., Manchester, W. B., Jin, M., & Vásquez, A. M. (2013). Evolution of the global temperature structure of the solar corona during the minimum between Solar Cycles 23 and 24. *The Astrophysical Journal*, *773*(1), 9. https://doi.org/10.1088/0004-637X/773/1/9

Nuevo, F. A., Vásquez, A. M., Landi, E., & Frazin, R. (2015). Multimodal differential emission measure in the solar corona. *The Astrophysical Journal*, *811*(2), 128. https://doi.org/10.1088/0004-637X/811/2/128

Ofman, L. (2010). Wave modeling of the solar wind. *Living Reviews in Solar Physics*, *7*(1), 4. https://doi.org/10.12942/lrsp-2010-4

Oran, R., Landi, E., van der Holst, B., Lepri, S. T., Vásquez, A. M., Nuevo, F. A., et al. (2015). A steady-state picture of solar wind acceleration and charge state composition derived from a global wave-driven MHD model. *The Astrophysical Journal*, *806*(1), 55. https://doi.org/10.1088/0004-637X/806/1/55

Powell, K. G., Roe, P. L., Linde, T. J., Gombosi, T. I., & De Zeeuw, D. L. (1999). A solution-adaptive upwind scheme for ideal magnetohydrodynamics. *Journal of Computational Physics*, *154*(2), 284–309. https://doi.org/10.1006/jcph.1999.6299

Sachdeva, N., Tóth, G., Manchester, W. B., van der Holst, B., Huang, Z., Sokolov, I. V., et al. (2021). Simulating Solar Maximum Conditions Using the Alfvén Wave Solar atmosphere Model (AWSoM). *The Astrophysical Journal*, *923*(2), 176. https://doi.org/10.3847/1538-4357/ac307c

Sachdeva, N., van der Holst, B., Manchester, W. B., Tóth, G., Chen, Y., Lloveras, D. G., et al. (2019). Validation of the Alfvén wave solar atmosphere model (AWSoM) with observations from the low corona to 1 Au. *The Astrophysical Journal*, *887*(1), 83. https://doi.org/10.3847/1538-4357/ab4f5e

Schiff, A. J., & Cranmer, S. R. (2016). Explaining inverted-temperature loops in the quiet solar corona with magnetohydrodynamic wave-mode conversion. *The Astrophysical Journal*, *831*(1), 10. https://doi.org/10.3847/0004-637X/831/1/10

Shi, T., Manchester, I., WardLandi, E., van der Holst, B., Szente, J., Chen, Y., et al. (2022). AWSoM Magnetohydrodynamic Simulation of a Solar active Region with Realistic Spectral Synthesis. *The Astrophysical Journal*, *928*(1), 34. https://doi.org/10.3847/1538-4357/ac52ab

Sittler, E. C., Jr., & Guhathakurta, M. (1999). Semiempirical two-dimensional magnetohydrodynamic model of the solar corona and interplanetary medium. *The Astrophysical Journal*, *523*(2), 812–826. https://doi.org/10.1086/307742

Sokolov, I. V., van der Holst, B., Oran, R., Downs, C., Roussev, I. I., Jin, M., et al. (2013). Magnetohydrodynamic waves and coronal heating: Unifying empirical and MHD turbulence models. *The Astrophysical Journal*, *764*(1), 23. https://doi.org/10.1088/0004-637X/764/1/23

Suess, S. T., Ko, Y. K., von Steiger, R., & Moore, R. L. (2009). Quiescent current sheets in the solar wind and origins of slow wind. *Journal of Geophysical Research*, *114*(A4), A04103. https://doi.org/10.1029/2008JA013704

Thernisien, A. F., & Howard, R. A. (2006). Electron density modeling of a streamer using LASCO data of 2004 January and February. *The Astrophysical Journal*, *642*(1), 523–532. https://doi.org/10.1086/500818

Tóth, G., van der Holst, B., Sokolov, I. V., De Zeeuw, D. L., Gombosi, T. I., Fang, F., et al. (2012). Adaptive numerical algorithms in space weather modeling. *Journal of Computational Physics*, *231*(3), 870–903. https://doi.org/10.1016/j.jcp.2011.02.006

van der Holst, B., Manchester, W. B., Frazin, R. A., Vásquez, A. M., Tóth, G., & Gombosi, T. I. (2010). A data-driven, two-temperature solar wind model with Alfvén waves. *The Astrophysical Journal*, *725*(1), 1373–1383. https://doi.org/10.1088/0004-637X/725/1/1373

van der Holst, B., Sokolov, I. V., Meng, X., Jin, M., Manchester, W. B., Tóth, G., & Gombosi, T. I. (2014). Alfvén wave solar model (AWSoM): Coronal heating. *The Astrophysical Journal*, *782*(2), 81. https://doi.org/10.1088/0004-637X/782/2/81

Van Doorsselaere, T., Srivastava, A. K., Antolin, P., Magyar, N., Vasheghani Farahani, S., Tian, H., et al. (2020). Coronal heating by MHD waves. *Space Science Reviews*, *216*(8), 140. https://doi.org/10.1007/s11214-020-00770-y

Vásquez, A. M. (2016). Seeing the solar corona in three dimensions. *Advances in Space Research*, *57*(6), 1286–1293. https://doi.org/10.1016/j.asr.2015.05.047

Vásquez, A. M., Frazin, R. A., & Kamalabadi, F. (2009). 3D temperatures and densities of the solar corona via multi-spacecraft EUV tomography: Analysis of prominence cavities. *Solar Physics*, *256*(1–2), 73–85. https://doi.org/10.1007/s11207-009-9321-1

Vásquez, A. M., Frazin, R. A., Manchester, I., & Ward, B. (2010). The solar minimum corona from differential emission measure tomography. *The Astrophysical Journal*, *715*(2), 1352–1365. https://doi.org/10.1088/0004-637X/715/2/1352

Vásquez, A. M., Huang, Z., Manchester, W. B., & Frazin, R. A. (2011). The WHI corona from differential emission measure tomography. *Solar Physics*, *274*(1–2), 259–284. https://doi.org/10.1007/s11207-010-9706-1

Vibert, D., Peillon, C., Lamy, P., Frazin, R. A., & Wojak, J. (2016). Time-dependent tomographic reconstruction of the solar corona. *Astronomy and Computing*, *17*, 144–162. https://doi.org/10.1016/j.ascom.2016.09.001

Wang, T., Reginald, N. L., Davila, J. M., St Cyr, O. C., & Thompson, W. T. (2017). Variation in coronal activity from solar cycle 24 minimum to maximum using three-dimensional reconstructions of the coronal electron density from STEREO/COR1. *Solar Physics*, *292*(8), 97. https://doi.org/10.1007/s11207-017-1130-3

Wang, Y. M., & Sheeley, N. R., Jr. (1990). Solar wind speed and coronal flux-tube expansion. *The Astrophysical Journal*, *355*, 726. https://doi.org/10.1086/168805